Rotor / Wake Aerodynamics Assignment 1

Mustafa Sabri Güverte 4548361 & Austin Ramanna 4663314 & Anastasios Panagiotopoulos 5350522

Tuesday 5th April, 2022

Contents

Chapter 1

Introduction

Climate change is an enormous issue in our current world while the demand for power and transportation increase constantly. Hence, propellers are the future of sustainable aviation. Wind turbines have become the major renewable energy source. A zero-emission future is feasible based on the usage of propellers and turbines. Therefore, propeller and turbine aerodynamics are more relevant than ever before. Thus, the simulation of their performance is necessary. Blade Element Momentum (BEM) models are used widely to model propeller and wind turbine aerodynamics.The basic assumption of the Blade Element Momentum theory is that the force of a blade element is responsible for the change of momentum of the air which passes through the stream tube [Burton et al., 2021].The basic principle of BEM is to balance the loads between the stream tube and the blade element at each annulus ring investigated. The Actuator Disk momentum theory, which models the propeller as a one-dimensional element, is applied at the annulus to determine the induction as a function of the loading on the blade segment. For the scope of the assignment, a Blade Element Momentum (BEM) model is programmed. The BEM model evaluates the performance of a wind turbine, in different configurations. Finally, the assumptions and the results of this code follow in the next sections.

Chapter 2

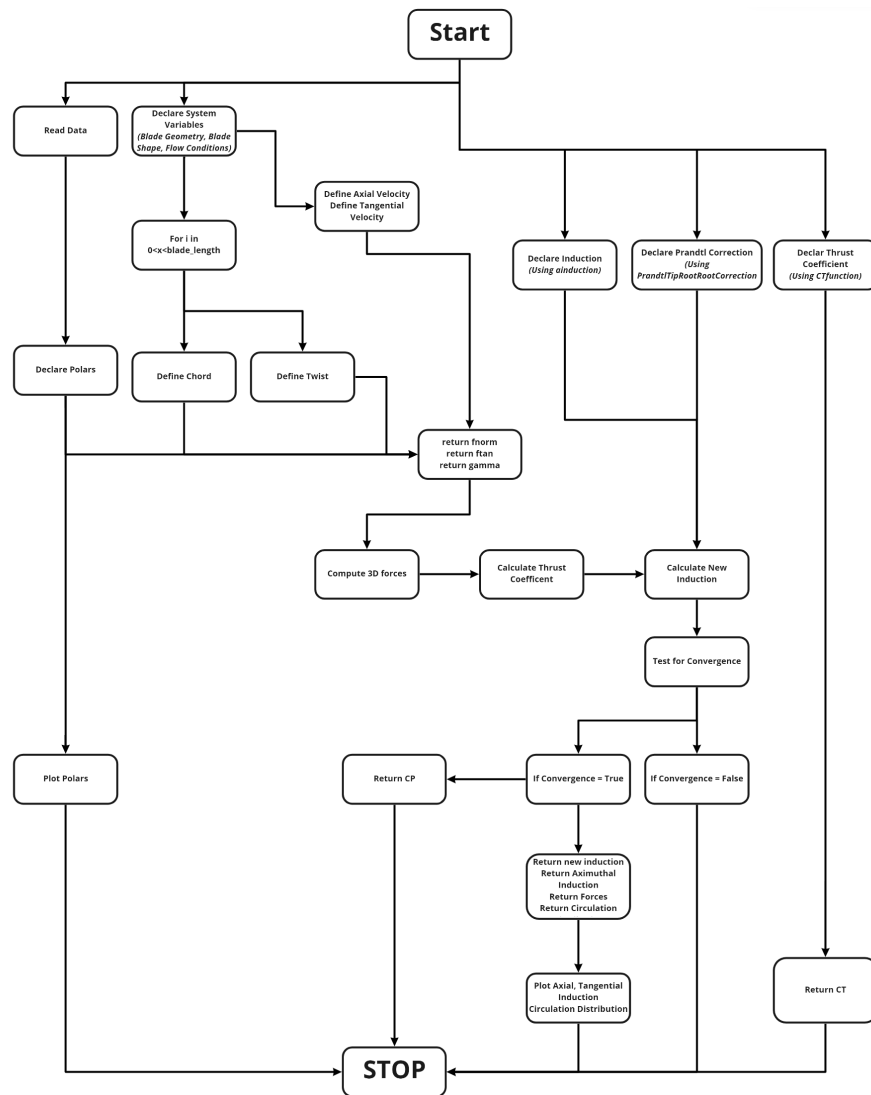# Flow chart

Figure 2.1 shows the flowchart of the python code.

Figure 2.1: Flow Chart of the Code

Chapter 3

Main assumptions

In order to feasibly solve the system, the following assumptions are employed. Firstly the flow is considered uniform and thus irrational over each annulus of the rotor disc. Furthermore the forces acting on the blade are assumed to be able to be modelled using the two dimensional airfoil characteristics, thus three dimensional forces and spanwise velocity contributions are ignored. Furthermore, the basic assumption of blade element theory stipulates that the force induced by a section of the blade is solely responsible for the change in momentum experienced by the air. Furthermore no interactions between the radial component of the anulli and the air is considered.Furthermore, due to the impact of drag being limited to the wake, the drag coefficient is not considered in the below mentioned calculations. [Burton et al., 2021]

$$\frac{a}{1+a'} = \frac{\sigma_r C_y}{4\sin\phi\cos\phi} \tag{3.1}$$

where

$$\sigma_r = \frac{N}{2\pi}\frac{c}{r} = \frac{N}{2\pi\mu}\frac{c}{R} \tag{3.2}$$

Chapter 4

Results

In this section, the results for the Blade Element Momentum (BEM) are evaluated. The primary purpose is to compute the performance of the wind tunnel for three different tip speed ratios, in the axial flow case. Before the presentation of the results, the correction for heavily loaded rotors (Glauert's correction) is necessary in this case. Above a specific loading on the stream tube, the wake will enter a turbulent wake state [Ferreira, 2021a], and as a result, the original assumptions for thrust coefficient and axial are no longer valid. Thus, the impact of Glauert's correction for heavily loaded rotors is illustrated in Figure 4.1:


.
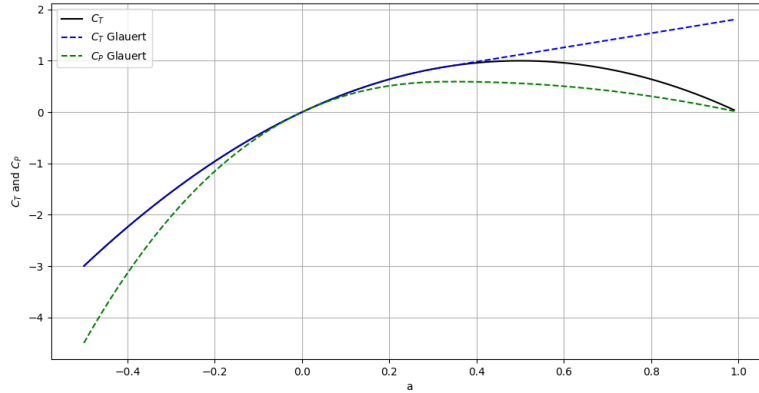
Figure 4.1: Variation of thrust and power coefficients with axial induction factor (a), with and without Glauert correction.

The first significant conclusion base on Figure 4.1, is that the corrected thrust coefficient deviates from the uncorrected value as the axial flow induction factor increase. Furthermore, until the value of $a \cong 0.4$, the results with and without the Glauert correction are identical. At this critical value ($a \cong 0.4$), the two thrust coefficients start to diverge and reach the maximum divergence as the inflow factor approach the value of 1, and thus, the correction for this area is necessary. Moreover, it is necessary to mention that for the inflow factor $-0.2 < a < 0.2$, the power

coefficient is similar to the uncorrected and corrected thrust coefficient. Finally, at the highest value of the axial flow factor, the power coefficient equals with thrust coefficient, without the Glauert correction.
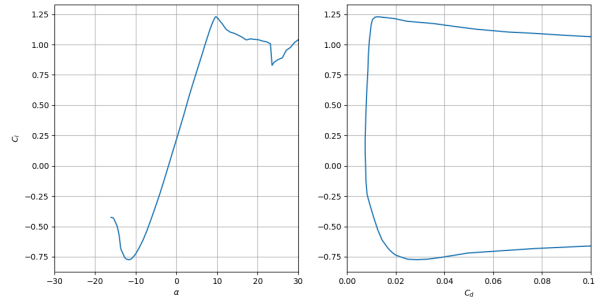
The plots of lift coefficient (C_l) versus the angle of attack (α) and lift coefficient versus drag coefficient (C_d), for the airfoil DU 95-W-180 of the wind turbine are following in Figure 4.2:
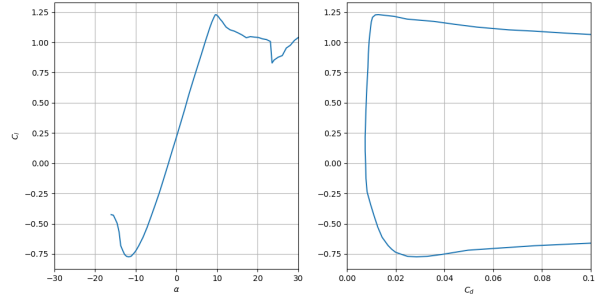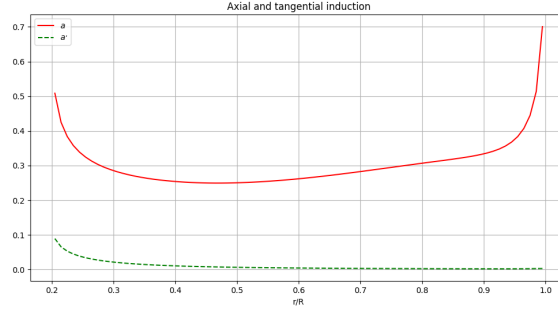

(a) TSR 10
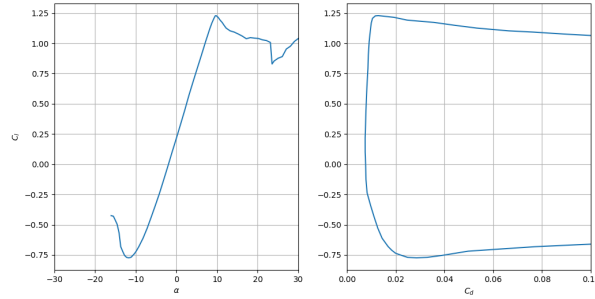
(b) TSR 8

(c) TSR 6

Figure 4.2: Lift coefficient vs. angle of attack (α) and lift vs. drag coefficient polars, for tip speed ratios: $TRS = 6$, $TRS = 8$ and $TRS = 10$.

From Figure 4.2, we can derive that the aerodynamic coefficients of the airfoil for tip speed ratios are identical. Hence, the aerodynamic performance of the air-

foil is independent of the tip speed ratio. In addition, the stall point appears at the angle of attack $\alpha \cong 10°$, as expected for this airfoil. The minimum value of drag coefficient appears at zero lift coefficient as expected from theory [Anderson Jr, 2010].
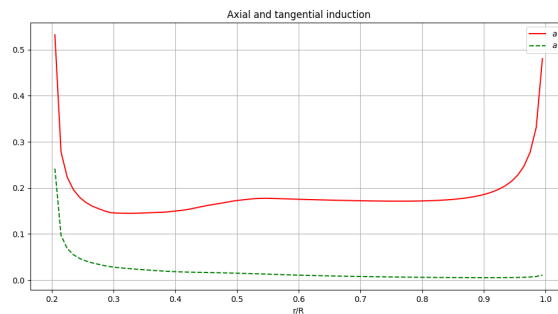
To continue with, the graphs for tangential and axial induction factor , versus the ratio of annular ring radius (r) to tip radius (R), are demonstrated in Figure 4.3:
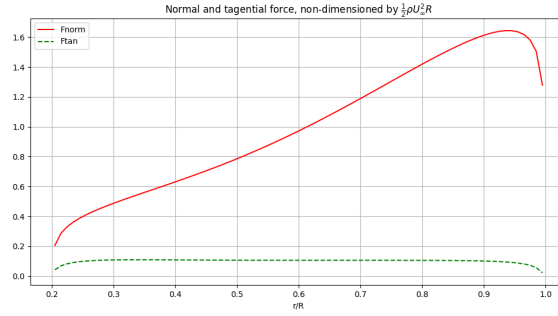

(a) TSR 10
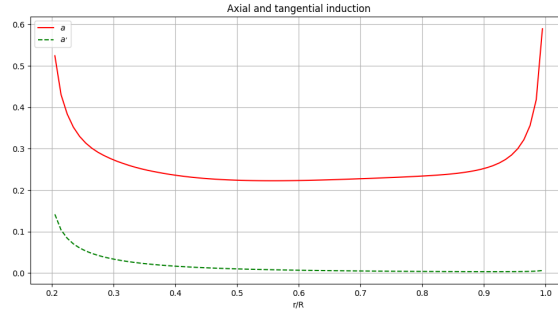
(b) TSR 8

(c) TSR 6

Figure 4.3: Tangential and axial induction factor, for tip speed ratios: $TRS = 6$, $TRS = 8$ and $TRS = 10$.

The first conclusion that we can derive from Figure 4.3 is that as the tip speed ratio increase, the average axial induction factor (a) increase, and the average tangential induction factor (a') decrease. Further, as the tips speed ratio decrease the maximum

axial induction factor moves from high r/R to low r/R ratios. The highest value for the axial induction equals $a \cong 0.7$, for $r/R \cong 1$ and tip speed ratio $TSR = 10$. On the other hand, the maximum tangential induction factor is $a' \cong 0.25$ and appears for $r/R \cong 0.2$ and tip speed ratio $TSR = 6$. The minimum inflow factor $a \cong 0.15$, for $r/R \cong 0.3$ and tip speed ratio $TSR = 6$. To conclude, the minimum tangential induction equals $a' \cong 0$ and can be found at a high r/R ratio for all configurations of tip speed ratio.
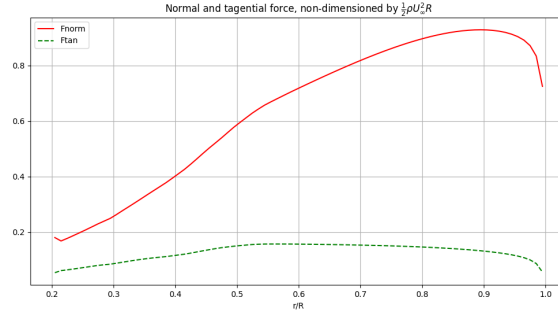
The plots for the non-dimensional normal and tangential force versus the ratio of annular ring radius (r) to tip radius (R) are following:
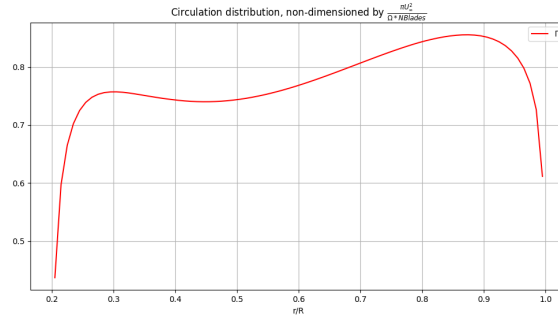

(a) TSR 10
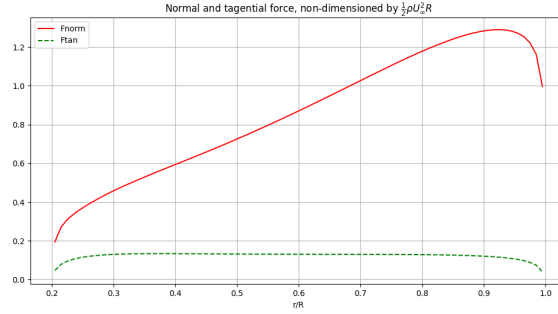
(b) TSR 8

(c) TSR 6

Figure 4.4: Normal and tangential force vs. r/R, for tip speed ratios: $TRS = 6$, $TRS = 8$ and $TRS = 10$.

Based on Figure 4.4, we obtain the expected behavior for the normal and tangential force. The normal force increase and the tangential force decrease as the tip speed ratio increase. The maximum of the normal force is $F_{norm} \cong 1.6$ and appear for $r/R \cong 0.95$ at $TSR = 10$. In contrast, the tangential force becomes maximum for $r/R \cong 0.55$ and $TSR = 6$. The minimum value for normal force equals $F_{norm} \cong 1.6$, while the minimum tangential force is zero, in all three configurations of tip speed ratio. Finally, the distribution of the forces looks similar in the case of $TSP = 10$ and $TSP = 8$, while some unsteadiness introduces for $TSP = 6$.
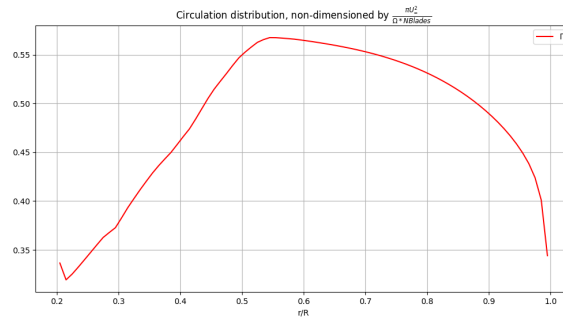
The next Figure 4.5 illustrates the non-dimensional circulation distribution versus the ratio r/R, for three different tip speed ratios:

(a) TSR 10
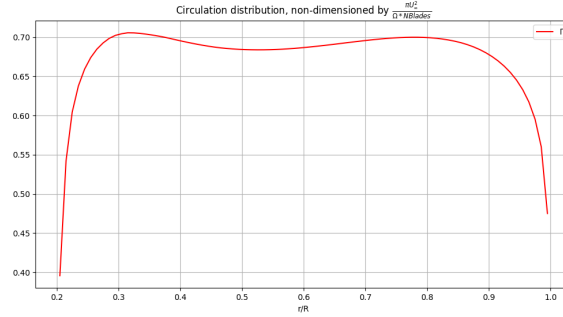
(b) TSR 8

(c) TSR 6

Figure 4.5: Circulation (Γ) vs. r/R, for the three tip speed ratios.

The first important remark derived by Figure 4.5 is that the circulation decrease as the tip speed ratio decrease. As the tip speed ratio decrease, the angular position of the maximum circulation moves from the tip to the root of the wing turbine. The maximum value of circulation is $\Gamma \cong 0.89$, for $r/R = 0.9$ and $TSR = 10$. On the other hand, the minimum $\Gamma \cong 0.32$, for $r/R \cong 0.22$ and $TSR = 6$. The circulation distribution looks similar in the case of $TSP = 10$ and $TSP = 8$, while some fluctuations introduce for $TSP = 6$.

In conclusion, the total thrust and power coefficients at the stream tube, for the three different configurations are represented in Table 4.1

Table 4.1: Coefficients

Tip speed ratio (TSR)	6	8	10
Thrust coefficient (C_T)	0.489	0.655	0.764
Power coefficient (C_P)	0.363	0.448	0.458

Taking everything into consideration, the maximum thrust appears for a tip speed ratio of $TSR = 10$ and the minimum thrust can be found for a tip speed ratio of $TSR = 6$, as expected. In the case of the power coefficient, the values for $TSR = 8$ and $TSR = 10$ are similar, while the minimum noticed for $TSR = 6$.
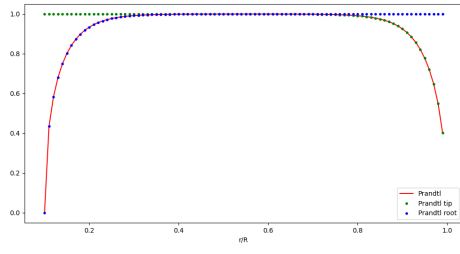
Chapter 5

Tip Correction

$$f\left(\frac{r}{R}\right) = \frac{2}{\pi} \arccos\left(e^{-\pi(1-r/R)/d}\right)$$
$$d = \frac{2\pi}{B} \frac{(1-a)}{\sqrt{\lambda^2 + (1-a)^2}}$$
(5.1)

$$f_T(\mu) = \frac{2}{\pi} \arccos\left(e^{-\frac{B}{2}\left(\frac{1-\mu}{\mu}\right)}\sqrt{1 + \frac{(\lambda\mu)^2}{(1-a)^2}}\right)$$
(5.2)

$$f_R(\mu) = \frac{2}{\pi} \arccos\left(e^{-\frac{B}{2}\left(\frac{\mu-\mu_R}{\mu}\right)\sqrt{1+\frac{(\lambda\mu)^2}{(1-a)^2}}}\right)$$
(5.3)

$$\Phi = \operatorname{atan}\left(\frac{1}{\lambda\mu}\frac{\left(1-\frac{a}{f}\right)}{\left(1+\frac{a'}{f}\right)}\right)$$
(5.4)

Equation 5.1 through Equation 5.4 shows the Prandtl corrections for the tip equation. The handbook states that this Prandtl approximation is possible because the vortex sheets are impermeable which makes them replaceable by material sheets. These would then upon travelling with the wake velocity have no effect on the wake [Burton et al., 2021]. The corrections are performed because there are a finite number of blades with a finite bound circulation; generating a finite tip vortex at the blade tip. The vortex creates an asymptotic induction invalidating the momentum balance approach and the Prandtl correction adjusts the balance for this induction. Figure 5.1 shows how the Prandtl tip correction is implemented. Note that the figures are nearly identical for all three TSR settings indicating that the turbine geometry plays the largest role in the correction strength. Another note is that the correction has a relatively strength at $r/R = 0.2$, the location where the blade starts; implying the correction has a significant effect on the results.

(a) TSR 10
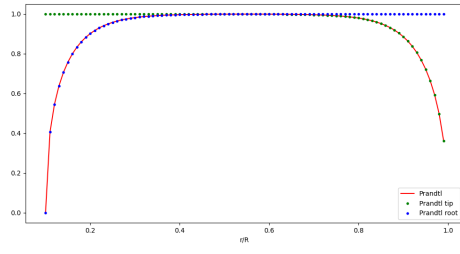
(b) TSR 8
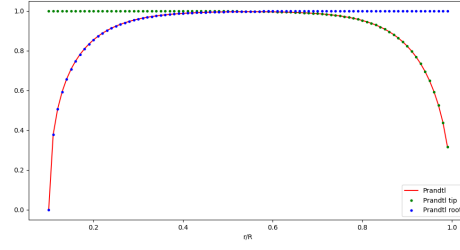
(c) TSR 6

Figure 5.1: Prandtl corrections

Chapter 6

Stagnation enthalpy

In this chapter the stagnation enthalpy in four different locations of the domain, is evaluated. These locations are at infinity upwind, at the upwind side of the rotor, at the downwind side of the rotor and infinity downwind. The Equation 6.1 is utilized for the computation of change of the stagnation enthalpy [Ferreira, 2021b]. The coordinate system is chosen cylindrical and can be observed in Figure 6.1[1]:

$$
\vec{\nabla} h_s = \begin{bmatrix} \frac{\partial h_s}{\partial r} \\ \frac{\partial h_s}{\partial \theta} \\ \frac{\partial h_s}{\partial z} \end{bmatrix} = \begin{bmatrix} v_\theta \omega_z - v_z \omega_\theta \\ -v_r \omega_z + v_z \omega_r \\ v_r \omega_\theta - v_\theta \omega_r \end{bmatrix} + \frac{1}{\rho} \begin{bmatrix} f_r \\ f_\theta \\ f_z \end{bmatrix} \tag{6.1}
$$
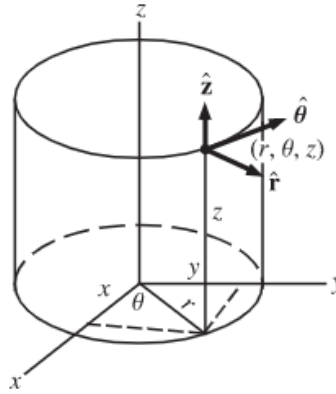
Figure 6.1: cylindrical coordinates

In Equation 6.1 h_s is the stagnation enthalpy, $\vec{v}$ is the velocity field, $\vec{\omega}$ is the vorticity, $\vec{f}$ is the force field in axial flow direction and ρ is the density of the air. As can be obtained from Equation 6.1 these vectors are calculated in cylindrical coordinates. We evaluate Equation 6.1 for the scope of our simplified problem, and as a result, it is simplified as follows in Equation 6.2:

---

[1]https://mechanicalland.com/explanation-of-the-cylindrical-coordinate-systems/

$$\frac{\partial h_s}{\partial r} = v_\theta \omega_z - v_z \omega_\theta + \frac{f_r}{\rho} \tag{6.2}$$

As one can see, the change in enthalpy is reduced to a function of azimuthal velocity $\vec{v}_\theta$ and vorticity $\vec{\omega_\theta}$, the axial velocity $\vec{v}_z$ and vorticity $\vec{\omega_z}$, the normal force $\vec{f_r}$ and the density ρ.
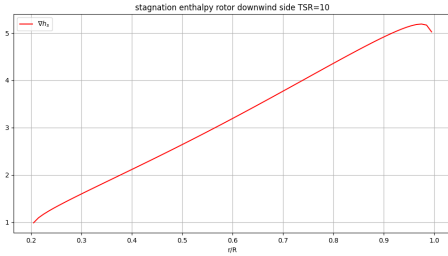
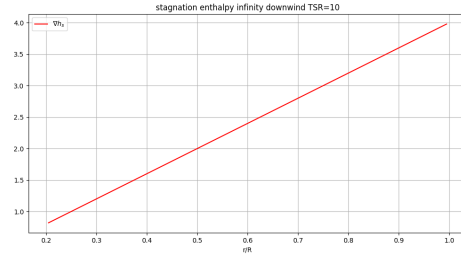The stagnation enthalpy as a function of radius, is illustrated in Figure 6.2, Figure 6.3 and Figure 6.4:
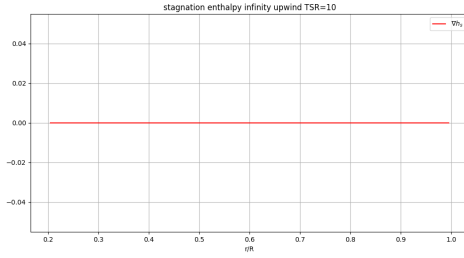
(a) Infinity upwind
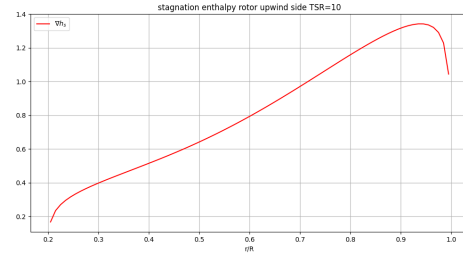
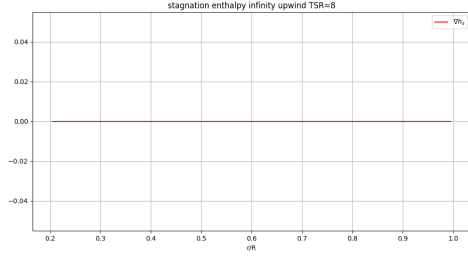**(b)** Upwind side of the rotor

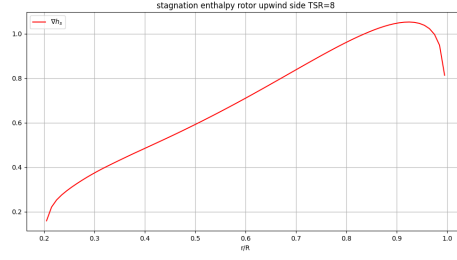**(c)** Downwind side of the rotor

(d) Infinity downwind

Figure 6.2: Stagnation enthalpy vs. r/R, for TSR=10

(a) Infinity upwind

(b) Upwind side of the rotor

(c) Downwind side of the rotor

(d) Infinity downwind
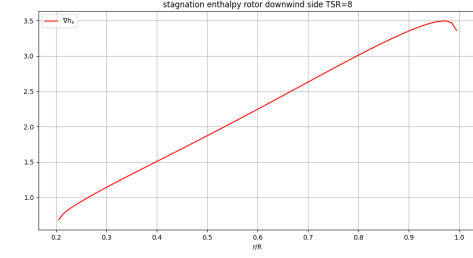
Figure 6.3: Stagnation enthalpy vs. r/R, for TSR=8
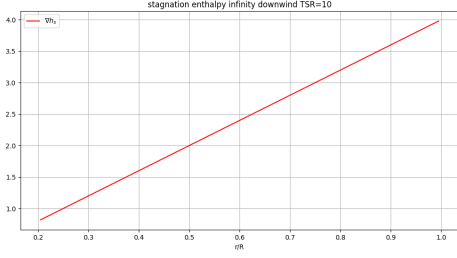

(a) Infinity upwind

(b) Upwind side of the rotor
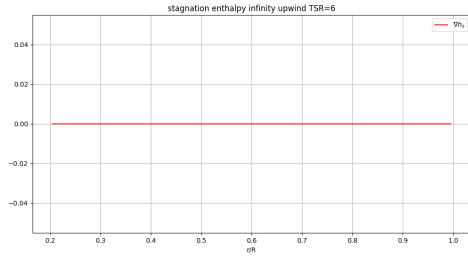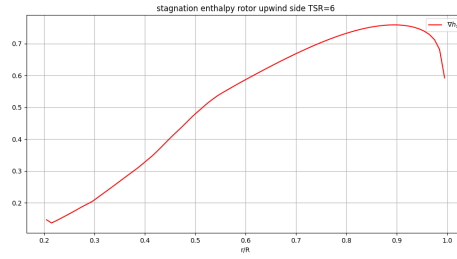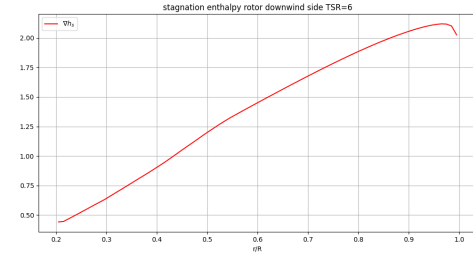
(c) Downwind side of the rotor
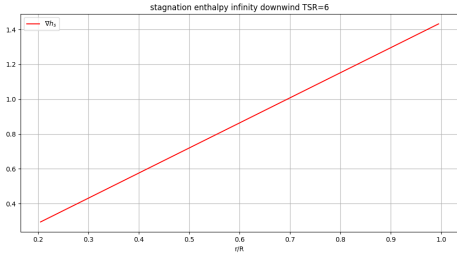
(d) Infinity downwind

Figure 6.4: Stagnation enthalpy vs. r/R, for TSR=6

Looking at Figure 6.2 and Figure 6.4, the first observation one makes is that the change in enthalpy for the infinite upwind is zero. This is attributed as the flow is considered irrotational and the body forces have yet to act on the air. Once the flow reaching the upwind side of the motor, only the force acts on the still irrotational

air. At the downwind side of the rotor, the flow still experiences the force generated by the blade but now the flow is also rotational causing the largest magnitudes of enthalpy change. Finally at the far downwind, the flow is still rotational yet the flow does not experience the blade forces. Looking at impact of TSR, one sees a positive correlation with the enthalpy change, the magnitudes increase from TSR from six to eight. The changes are much less pronounced from eight to ten.

Chapter 7

Operational point

From Table 4.1 in chapter 5 it can be observed that the C_p is highest at a TSR of 10. Note that just like the specific enthalpy the just from 8 to 10 is smaller than from 6 to 8; suggesting the approach of a maximum. Furthermore, performing a run at TSR of 12 returns a CT of 0.847 which is higher than the 0.764. Therefore at TSR equals 10 $a < \frac{1}{2}$ making a TSR of 10 highly feasible. The TSR of 10 is further supported by the force distributions from Figure 4.3 through Figure 4.5 where this ratio produces the highest forces. The wind energy handbook states that a high rpm is beneficial at high speeds as it can extract more power but suffers at low speeds due to higher drag [Burton et al., 2021]. It could thus be argued that at a lower U0, a lower TSR is desired.

Chapter 8

Discussion and Conclusion

Based on chapter 4, the BEM model which developed seems to work better in the case of tip speed ratios of $TSR = 8$ and $TSR = 10$, while some instabilities introduce for $TSR = 6$. This phenomenon (fluctuations) is mainly caused by the fact that the inflow induction factor is non-uniform in low TSR configurations. Moreover, the circulation distribution for tip speed ratio equals $TSR = 6$ is non-uniform. Hence, the model fails to predict the radial interaction and the exchange of momentum, while utilizing low TSR configurations. The BEM is proposed for large values of tip speed ratio. Regarding the operational point, it was noted that the pressure coefficient was the largest at a TSR of 10 thus giving the operational point, it is however noteworthy to state that at lower U_0, a lower TSR would be preferred.

Bibliography

[Anderson Jr, 2010] Anderson Jr, J. D. (2010). *Fundamentals of aerodynamics*. Tata McGraw-Hill Education.

[Burton et al., 2021] Burton, T., Jenkins, N., Sharpe, D., Bossanyi, E., and Graham, M. (2021). *Wind energy handbook*. Wiley.

[Ferreira, 2021a] Ferreira, C. (2021a). BEM - Blade element momentum theory. Online.

[Ferreira, 2021b] Ferreira, C. (2021b). Stagnation enthalpy and total pressure across an actuator and wake. Online.